ACCSCIENCE PUBLISHING

International Journal of Bioprinting

RESEARCH ARTICLE

Magnetically programmable 3D printing of liquid metal robots for targeted therapy

Weichen Feng[1†], Xiaohui Shan[1†], Minghui Guo[2], Bo Wang[3], Xiyu Zhu[4], Bo Yuan[5], Jianye Gao[2*], and Jing Liu[1,2*]

[1]Medical Microsystems Laboratory, School of Biomedical Engineering, Tsinghua University, Beijing, China

[2]State Key Laboratory of Cryogenic Science and Technology and Beijing Key Laboratory of Cryobiomedicine, Technical Institute of Physics and Chemistry, Chinese Academy of Sciences, Beijing, China

[3]Center of Double Helix, Tsinghua Shenzhen International Graduate School, Tsinghua University, Shenzhen, China

[4]Research Institute of Petroleum Processing, SINOPEC, Beijing, China

[5]Department of Mechatronics Engineering and Automation, School of Mechanical Engineering and Automation, Beihang University, Beijing, China

Abstract

Magnetic liquid metal soft robots hold promise for minimally invasive interventions in complex *in vivo* environments, yet their fabrication challenges must simultaneously achieve structural customization, spatial magnetic programming, and rapid conductive network construction. Here, we present a magnetic-field-assisted 3D printing strategy to fabricate soft robots with programmable magnetic domains and magnetothermal therapeutic capabilities. Using acid-assisted de-oxidation and silver (Ag)-coated neodymium–iron–boron (NdFeB) particles to enhance wetting, we prepared magnetic liquid metals that exhibit magnetic-field-induced coalescence and achieved an order-of-magnitude increase in electrical conductivity. Furthermore, a geometry-dependent model based on eddy-current losses revealed that printed paths significantly improve heating efficiency under alternating magnetic fields. Leveraging a locally oriented magnetic field during printing, we encoded spatially resolved hard-magnetic domains, yielding predictable 3D deformation and multiple gaits, including grasping, crawling, and rolling. Finally, we demonstrated localized magnetothermal heating in *ex vivo* porcine colon tissues, validated by thermal measurements and finite-element simulations. This study offers a manufacturable, programmable, and scalable liquid metal additive manufacturing platform for personalized magnetically driven magnetothermal therapy in complex biological environments.

Keywords: Liquid metals; Soft robots; Magnetically programmable 3D printing; Magnetothermal therapy

†*These authors contributed equally to this work.*

***Corresponding authors:**
Jianye Gao
(gaojianye@mail.ipc.ac.cn)
Jing Liu
(jliu@mail.ipc.ac.cn)

Citation: Feng W, Shan X, Wang B, *et al.* Magnetically programmable 3D printing of liquid metal robots for targeted therapy. *Int J Bioprint.* 2026;12(3):026180155.
doi: 10.36922/IJB026180155

Received: April 28, 2026

Revised: May 21, 2026

Accepted: May 25, 2026

Published online: May 25, 2026

1. Introduction

In recent years, intelligent robots have emerged as a transformative platform in biomedical applications, owing to their unprecedented capabilities in sensing, locomotion, and manipulation.[1-3] However, conventional rigid robots, while precise,

face inherent limitations in intimate interaction with soft, dynamic biological systems. Their mechanical stiffness, orders of magnitude higher than that of native tissues, poses a significant risk of iatrogenic injury, compromising both safety and patient comfort.[4,5] This concern has motivated the development of soft robotics.[6] Constructed from compliant materials, soft robots exhibit tissue-like compliance, remarkable deformability, and the capacity for extreme miniaturization to millimeter scales, making them particularly attractive for biomedical applications.[7,8] Despite these promising features, the field still confronts several challenges that hinder its clinical translation. Key issues include the complexity of controlling their deformation, the limited range of achievable shapes and structures, and the difficulty of integrating multiple functions into a single device. Achieving a combination of biocompatibility, ease of fabrication, and multifunctional performance remains a significant hurdle for soft robots to reach their full potential in the biomedical arena.[9,10]

Room-temperature liquid metals (LMs), such as gallium-based and bismuth-based alloys, combine high electrical and thermal conductivity with fluid-like deformability, and have demonstrated excellent biocompatibility in numerous studies.[11,12] These properties, together with their versatile functional performance, establish LMs as an emerging star material with significant potential in biomedicine.[13-16] When integrated with magnetic particles (e.g., neodymium–iron–boron [NdFeB], iron, or nickel), LMs can function as miniature soft robots, enabling manipulation through external magnetic fields.[17,18] Moreover, owing to their high metallic conductivity, magnetic LMs (MLMs) exhibit efficient eddy-current heating under alternating magnetic field (AMF), a feature widely exploited for the targeted thermal ablation of biological tissues.[19] The inherent flexibility and manoeuvrability of MLMs further allow minimally invasive access to biological environments, enabling medical functions such as contrast-enhanced imaging[20] and targeted drug delivery.[21] Consequently, MLMs show considerable promise for therapeutic applications.

However, the precision of MLM-mediated targeted therapy remains a challenge due to the non-structured, fluidic nature of LMs, which complicates spatial control and functional stability in dynamic physiological settings. To tackle the above challenges associated with shaping and controllably fabricating LMs, many manufacturing technologies have emerged. Among these, 3D printing stands out due to its advantages in customization, programmability, and precise controllability. It has demonstrated robust performance in flexible electronics, health monitoring, soft robotics, and energy management, highlighting its broad applicability.[22-24] However, most studies on MLM soft robots rely on conventional fabrication routes, which typically yield limited field-distribution modes and require relatively complex processing. For example, LM-bonded NdFeB can be fabricated at low temperatures and reconfigured for use in sensors and robotics.[25] Reprogrammable magnetic soft robots based on low-melting-point alloys encapsulate NdFeB particles within the alloy and achieve their orientation reconfiguration through thermally assisted solid-liquid phase transitions.[26] These approaches still rely on thermal reprogramming and mold-based composite fabrication, and the magnetic domain distribution cannot be directly written in sync with the robot's geometry. Meanwhile, spatial ferromagnetic-domain printing has been established as a powerful strategy for programming the deformation of hard-magnetic soft materials. Kim *et al.*[27] demonstrated that a nozzle-mounted permanent magnet could align hard-magnetic particles during printing, thereby encoding spatially resolved magnetic domains in an elastomer matrix. However, such hard-magnetic elastomer systems are primarily designed for programmable actuation and are generally non-conductive, which may restrict their potential for functional integration, such as AMF-induced eddy-current heating. Extending magnetic-domain printing from non-conductive elastomers to liquid-metal-containing conductive composites would therefore enable a different level of functional integration: The printing path could program not only magnetic actuation but also conductive-network geometry and magnetothermal performance.

Here, we proposed a magnetic-field-assisted direct ink writing (DIW) 3D printing strategy to encode magnetic-domain structures in MLM–elastomer (MLME) composites, enabling wireless locomotion in complex *in vivo* environments, such as the gastrointestinal tract. The approach exploits the field-induced coalescence of MLM droplets—a phenomenon that simultaneously establishes electrical interconnection without requiring conductive fillers or post-sintering steps[28], thereby eliminating reliance on costly noble metal fillers (e.g., Ag or Cu) and bypassing the complexities of conventional sintering.[29] In this conductive state, the MLM generates eddy currents under an AMF, permitting tumor thermal ablation. Furthermore, to enhance magnetothermal heating performance, we investigated the influence of printing toolpaths on magnetothermal efficiency, demonstrating that 3D printing can be leveraged not merely as a shaping tool, but as a means to program functional performance. Collectively, these strategies establish a scalable route for personalized magnetic actuation and magnetothermal therapy in anatomically complex *in vivo* environments.

2. Materials and methods

2.1. Materials

The eutectic gallium–indium alloy (EGaIn) was prepared by mixing 75.5 wt. % Ga and 24.5 wt. % In at 120 °C for 2 h. Silver-coated NdFeB microparticles (NdFeB@Ag) were purchased from Guangdong Meituo New Material Technology Co., Ltd (China). The elastomer matrix was prepared by mixing SE1700 (Dow Corning Corp., United States [US]) and polydimethylsiloxane (PDMS; Sylgard 184, Dow Corning Corp.) at a 2:1 volume ratio. HCl was purchased from Beijing Lanyi Chemical Products Co., Ltd (China). The pork intestines were purchased at a local supermarket.

2.2. Preparation of magnetic liquid metal–elastomer

The preparation process of MLME is illustrated in Figure 1a. Firstly, EGaIn and NdFeB@Ag microparticles were mixed at a mass ratio of 3:1 and stirred in 2 mol/L HCl to remove the oxide layer, yielding MLM once the magnetic particles were completely encapsulated. The acid-assisted mixing was completed in approximately 1 min, after which the obtained MLM was immediately rinsed with deionized water and dried to reduce prolonged acid exposure of the NdFeB@Ag particles. Subsequently, it was incorporated into the elastomer matrix at prescribed volume fractions to form the MLME ink, which was degassed to remove bubbles. Prior to printing, the ink was magnetized using an impulse magnetizer (ME-12150, MAGELE TECHNOLOGY (SHANGHAI) Co., LTD., China). The magnetic field strength used for this pre-magnetization step was 2 T, and the field was applied along the axial direction of the magnetizer coil/sample chamber. A printing head, controlled by G-code generated by the Python script, deposited the ink into the desired structures. All printed samples were cured at 90 °C for 2 h.

2.3. Material characterization

Morphological observations were performed using a scanning electron microscope (SEM) and energy-dispersive X-ray spectroscopy (EDS; SU-8600, Hitachi, Japan). Electrical properties were measured via a two-probe method using an inductance–capacitance–resistance (LCR) meter (E4980A, Keysight, US). Rheological properties were assessed with a rheometer (MCR-302E, Anton Paar, Austria) equipped with a 25 mm parallel-plate geometry (PP25, Anton Paar). Optical micrographs were obtained using a metallographic microscope (ECLIPSE LV150, Nikon, Japan). Thermal conductivity and volumetric heat capacity were measured by a transient plane source instrument (TPS2500S, Hot Disk, Sweden). Density was determined via the Archimedes-displacement method, and the mass-specific heat capacity was calculated from volumetric heat capacity and density.

2.4. Magnetothermal setup

The AMF heating was generated by an induction coil system (ZDBT-2, Hanggong Electric Technology, China). Samples were placed at the coil center, and their surface temperature evolution was monitored with an infrared camera (Fotric 268D, Germany). The $\Delta T(t)$ curves were extracted from the defined region of interest. All measurements were conducted under identical ambient conditions to minimize convection variability, with each experiment performed three times.

2.5. Magnetic-field-assisted direct ink writing system

A ring-shaped permanent magnet was mounted coaxially around the nozzle to provide a local magnetic field during extrusion (Figure S1), thereby aligning the hard-magnetic NdFeB@Ag particles along the printing direction and enabling spatially resolved magnetic encoding.

2.6. Finite-element thermal simulation

The heat transfer process between the MLME and intestinal tissue was numerically simulated using COMSOL Multiphysics 5.5 (Sweden). The equation was solved based on the finite element method. For the geometric model, the MLME (a cylinder with a diameter of 10 mm and height of 2 mm) was placed at the center of the cylindrical intestinal tissue (diameter 50 mm, height 2 mm). The heat transfer process was based on the following equation:

$$\rho C_p \frac{\partial T}{\partial t} = \nabla \left(k \nabla T \right) \tag{1}$$

where ρ is density, C_p is specific heat capacity, k is thermal conductivity, T is temperature, and t is time. The temperature change curve of the MLME was fitted using measured magnetothermal temperature-rise data from the MLME on a substrate with poor thermal conductivity. The initial temperature of the intestinal tissue was set to body temperature (37 °C). The mesh was divided into free tetrahedral elements. The output time step was 1 s, with a total duration of 180 s and a relative tolerance of 0.0001.

2.7. In vitro cytotoxicity assay

The *in vitro* cytotoxicity of the printed materials was evaluated using NIH 3T3 mouse embryonic fibroblasts. The samples were immersed in complete culture medium and incubated at 37 °C under constant shaking for 6 h to obtain extraction media. NIH 3T3 cells were seeded in 96-well plates and cultured in complete medium at 37

°C under 5% CO_2 for 24 h. The blank group contained no cells. The culture medium in the experimental groups was then replaced with the corresponding extraction media, followed by another 24 h of incubation. Subsequently, 10 μL of cell counting kit (CCK)-8 reagent was added to each well and incubated for 2 h. The optical density (OD) at 450 nm was measured using a microplate reader (Cytation, BioTek Instruments, US), and the cell viability was calculated relative to the control group. Live/dead staining was further performed and observed using confocal microscopy (FV3000, Olympus, Japan) to visualize cell survival after extract treatment.

3. Results and discussion

To formulate an LM ink with tunable rheology and stable printed structures, LMs are typically compounded with particles or polymers. However, LMs readily oxidize to form a surface oxide skin, and conventional mixing repeatedly fragments and re-oxidizes the droplets, compromising their intrinsic high electrical conductivity. Compared to traditional hard magneto-elastic inks, magnetic inks containing LM face additional challenges, including insulation between droplets caused by oxidation layers, possible separation of high-density components, and issues with rheological properties and print fidelity. Since the magnetothermal effect exploited here relies on eddy currents induced under an AMF, which demands a highly conductive composite, we employed acid-assisted mixing to continuously remove the oxide layer during processing. This strategy promotes wetting of magnetic particles on the LM surface and preserves conductivity after the composite is blended with a silicone elastomer. Notably, NdFeB particles are high-performance hard magnets but are susceptible to acid corrosion; therefore, surface modification offers an effective route for preparing MLM via acid mixing.[30] Here, we enhanced the interaction between NdFeB@Ag and LM by leveraging the ability of Ag to form intermetallic compounds at the LM interface. Based on SEM observations of the MLME surface morphology and the elemental distribution detected by EDS, we observed that the magnetic particles were encapsulated within the LM (Figure 1b). This acid-assisted mixing step is critical for subsequent magnetically assisted interconnection of LM droplets containing magnetic particles (Figure 1c). To stabilize the written magnetic programming, it is desirable to incorporate a high loading of NdFeB powder; however, excessive solid content reduces fluidity and hinders homogeneous dispersion. We found that a mass fraction of 25 wt. % NdFeB powder in MLM retained good flowability, and this formulation was therefore adopted throughout the study.

An MLM is intrinsically conductive, and its resistance remains low even with increased NdFeB loading (Figure S2). However, to obtain a printable and curable ink, MLM must be blended with a curable elastomer to form MLME. In elastomer matrices, LM droplets are often isolated by the polymer and cannot readily form continuous conductive pathways. Although magnetization can enhance the magnetic attraction between droplets in a directional field and promote percolation, a sufficiently high MLM content is nevertheless required to establish a stable conductive network in silicone rubber. We measured the electrical conductivity of MLME with different MLM volume fractions before and after magnetically induced sintering (n = 3). When the MLM volume fraction reached 40%, field-induced interconnection occurred, and the composite crossed the percolation threshold (Figure 2a). Increasing the MLM fraction to 45% enabled conductivity to rise to the order of 10^3 S/m under magnetic-field-induced sintering, sufficient to generate a pronounced temperature increase under AMFs via eddy-current heating. Optical metallography of the MLME surface revealed that, prior to applying the magnetic field, MLM droplets were dispersed and encapsulated by the silicone rubber, leaving numerous breaks that prevented the formation of a conductive loop (Figure 2bi). Upon magnetic-field exposure, the droplets underwent directional migration and coalescence, resulting in large connected LM domains and electrical continuity (Figure 2bii), with conductivity increasing by nearly eight orders of magnitude. Notably, this interconnection was irreversible after field removal; the MLME remained sintered and did not return to the insulating state. This irreversibility is attributed to the relatively large droplet size (~100 μm) and the highly viscous SE1700 silicone matrix, which imposes a large mechanical resistance to the re-separation of connected droplets.

After identifying the conductive volume fraction window, we evaluated the rheological properties required for DIW. MLME inks were prepared by mixing MLM with the high viscosity elastomer at different volume ratios. Viscosity measurements showed that viscosity increased markedly with MLM volume fraction, and all formulations exhibited pronounced shear-thinning behavior (Figure 2ci), which facilitates flow through the nozzle while allowing rapid shape retention after deposition. At a fixed shear frequency of 10 rad/s, amplitude sweeps of the storage modulus (G') and loss modulus (G") revealed that G' exceeded G" at low strain but crossed over at higher strain (Figure 2cii). This crossover (yield point) indicates a transition from elastic-dominated to flow-dominated behavior, suggesting that the ink can flow under applied stress and recover a solid-like state once the stress is removed. Both overly high and low MLM

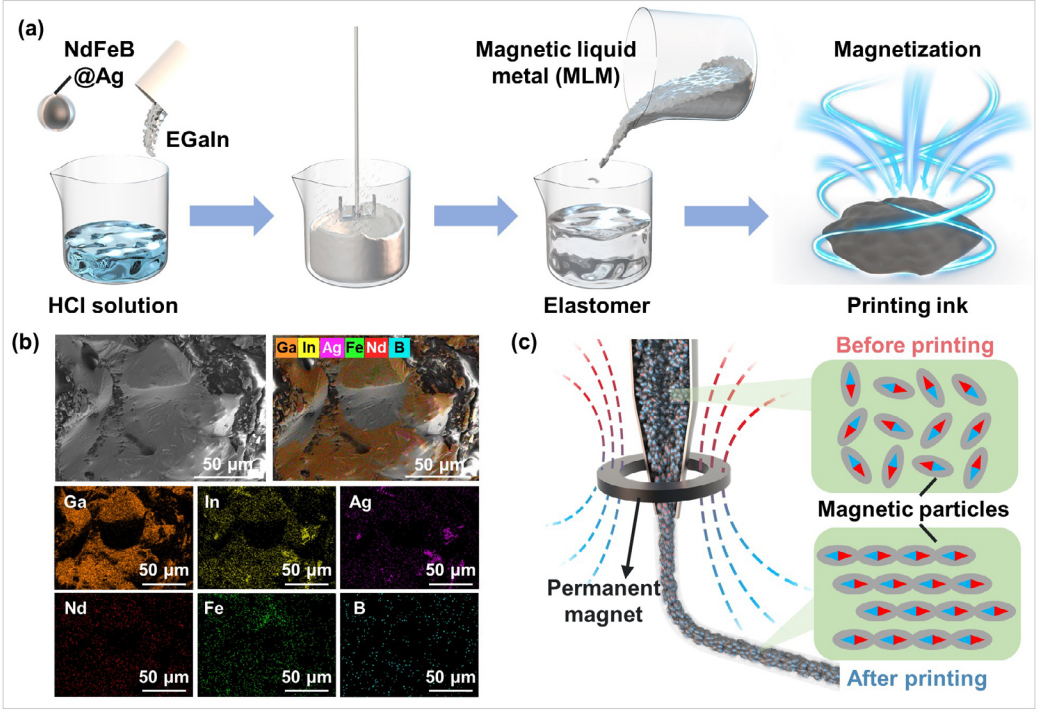

Figure 1. Magnetic field-assisted 3D printing of magnetic liquid metal elastomer. (a) Preparation process of MLME printing ink. (b) SEM and EDS results of MLME. Scale bars: 50 μm; magnifications: 800×. (c) Schematic diagram of the magnetic field-assisted DIW 3D printing principle.
Abbreviations: DIW: Direct ink writing; EDS: Energy-dispersive X-ray spectroscopy; EGaIn: Eutectic gallium–indium; MLME: Magnetic liquid metal–elastomer; NdFeB: Neodymium–iron–boron; SEM: Scanning electron microscopy.

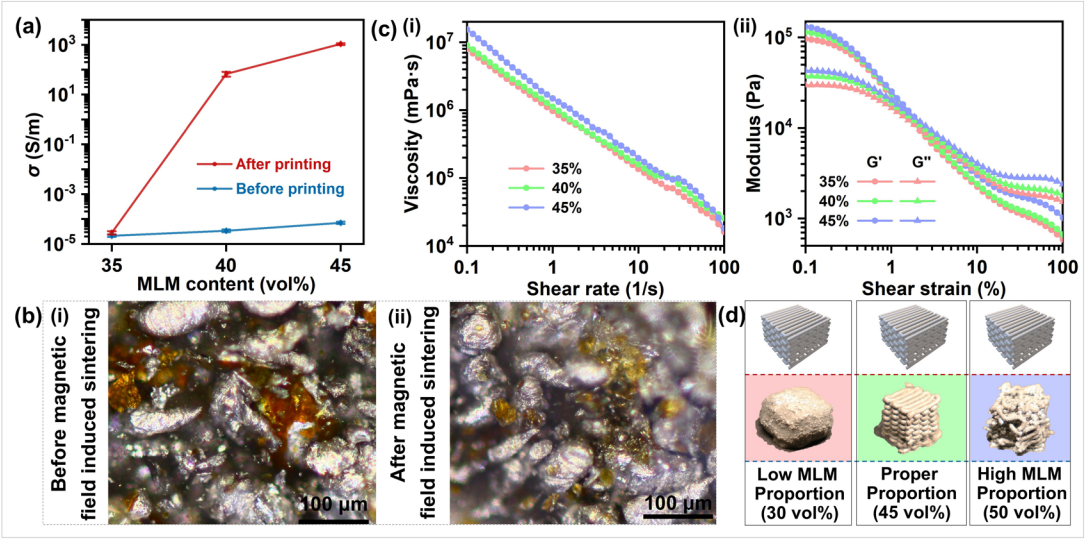

Figure 2. Characterization of MLME with varying MLM volume fractions. (a) Comparison of MLME electrical conductivity before and after printing at different MLM volume ratios (n = 3). (b) Optical micrographs of MLME (scale bars: 100 μm; magnifications: 10×). (i) Before magnetic-field-induced sintering. (ii) After magnetic-field-induced sintering. (c) (i) Viscosity of MLME at different MLM volume ratios. (ii) Modulus of MLME as a function of shear strain at different MLM volume ratios (shear frequency = 10 rad/s). (d) Photographs of printed samples with proper MLM ratio and improper conditions.
Abbreviations: MLM: Magnetic liquid metal; MLME: Magnetic liquid metal–elastomer.

fractions compromise print fidelity: Excessive MLM led to too high viscosity and unstable extrusion, causing path deviation and structural collapse, whereas insufficient MLM yielded low viscosity, resulting in filament spreading and poor shape formation. Only an appropriate MLM fraction enabled stable, self-supporting prints (Figure 2d). Considering both electrical and rheological results, we selected an MLM volume fraction of 45% as the default ink formulation, balancing printability and conductivity.

Moreover, we analyzed how printing methods affect the magnetothermal efficiency of MLME. In 3D printing, G-code specifies position and motion commands, providing substantial freedom to design printing directions and travel distances (**Video S1**). We first compared three representative printing paths—serpentine lines, an Archimedean spiral, and concentric closed loops (Figure 3a and 3b)—while keeping the printed part's outer dimensions and volume/mass constant. The results show that concentric closed-loop paths yielded significantly higher temperature-rise efficiency under AMF excitation than either the serpentine line toolpath or the Archimedean spiral. This trend is evident from the infrared temperature maps at identical time points, and is further confirmed by the ΔT-time curves obtained from repeated tests (n = 3).

To rationalize this difference, we derived an interpretable geometric factor model from the eddy-current power-loss expression. Under AMF excitation, electromagnetic induction generated eddy currents inside the conductor, and the associated energy dissipation was essentially Joule heating. The total eddy current loss power P can be expressed as the volume integral of current density $\boldsymbol{J}$ and conductivity σ over the conductor volume V:

$$P = \int_V \frac{\boldsymbol{J}^2}{\sigma} \mathrm{d}V \tag{2}$$

To incorporate the effect of geometry, the expression can be further simplified. For the line-like conductive traces produced by DIW in this work, each approximately closed printed path can be modeled as an equivalent conductive loop with cross-sectional area S, path length l, and enclosed area A. Under a sinusoidal magnetic field ($B = B_0 \sin \omega t$, where B_0 is the magnetic field amplitude, and ω is the angular frequency) perpendicular to the printing plane, Faraday's law gives the induced electromotive force in the loop as:

$$\varepsilon(t) = -\frac{d\Phi}{dt} = -A\frac{dB}{dt} = -AB_0\omega\cos\omega t \tag{3}$$

where ε is the induced electromotive force, and Φ is the magnetic flux. Given that the printed traces were line-like conductors, substituting the resistance relation and considering steady state sinusoidal excitation yielded the time-averaged power $\bar{P}$ over one period as:

$$\bar{P} = \frac{1}{2} I_0^2 R = \frac{\sigma B_0^2 \omega^2 A^2 S}{2l} \tag{4}$$

From the above, the dependence of eddy-current loss on geometric parameters can be summarized by a positive correlation with a geometry factor $\frac{A^2 S}{l}$. A larger loop area, a larger cross-section, and a shorter path length lead to stronger eddy-current heating. Because the trace cross-section is essentially the same for different paths in our experiments, the eddy-current loss is governed primarily by $\frac{A^2}{l}$. Therefore, for a given characteristic radius (i.e., comparable enclosed area), closed loops dominated conductive pathways are expected to be more favorable for eddy-current circulation because they provide a larger effective magnetic-flux enclosure and shorter characteristic current paths. In contrast, designing a single long non-closed spiral increases the effective path length without increasing the enclosed area, inevitably lowering heating efficiency; thus, concentric closed loops should outperform an Archimedean spiral. The superiority over a serpentine pattern is more intuitive: Arranging conductor length in directions that do not appreciably increase enclosed area (e.g., back-and-forth meanders) merely increases length without a corresponding increase in A, reducing the geometry factor.

It should be noted that **Equation 4** is a simplified geometry-based model derived from an ideal conductive loop. It is used to rationalize the relative heating trends across different printed patterns, rather than to quantitatively predict the exact eddy-current losses of the interconnected conductive network. Resistance measurements showed that, for low-filling concentric loop patterns, adjacent loops were physically separated and electrically insulated from each other. In contrast, for the 100% filled concentric loop pattern, the adjacent loops were electrically interconnected through contacts between neighboring filaments. Therefore, the 100% filled concentric-loop pattern should be regarded as an interconnected conductive network with loop-dominated geometry, rather than as a set of completely independent conductive loops. Under this condition, directly summing the contributions from individual loops may overestimate the absolute heating power. Nevertheless, the model remains valid for rationalizing the relative heating trend, because the concentric-loop pattern still provides efficient

closed-current circulation, large effective flux enclosure, and relatively short characteristic current paths. This explains the experimentally observed higher heating efficiency of the concentric-loop pattern, especially at higher filling ratios (Figure 3c and 3d). Finally, when comparing different outer shapes at a fixed loop area, the result follows from the isoperimetric inequality: among closed planar curves with the same perimeter, a circle encloses the maximum area (equivalently, for the same area, the circle has the shortest perimeter). Combined with the geometry factor, a circular outline therefore provides the highest magnetothermal efficiency, consistent with the infrared temperature maps of different shapes (Figure 3e and 3f). Overall, for localized magnetothermal ablation, the printed heater should adopt a circular outline with 100% fill rate and concentric closed loop paths to maximize the geometry factor—and thus heating efficiency—for a given size and material usage.

Next, we evaluated magnetic domain programming, which is essential for imparting programmable, customized actuation. By placing a ring-shaped permanent magnet near the printing head, we could define the magnetization orientation of the extruded filament through the printing direction.

To validate that the proposed domain-programming strategy enables predictable 3D deformation, we designed a long strip structure (Figure 4ai) and a radial six-arm structure (Figure 4bi), with the gray lines denoting the deposited filaments and the black arrows indicating the printing directions. We then compared their morphologies with and without an external magnetic field. In the absence of a magnetic field, all samples remained planar, indicating good shape stability in the absence of stimulation (Figure 4aii and 4bii). Upon applying an external magnetic field, the samples exhibited pronounced and repeatable deformations, with the deformation modes corresponding to the prescribed magnetization orientation (Figure 4aiii and 4biii). In the long-strip structure, oppositely magnetized domains along the length generated differential magnetic torques under an external field, inducing global curling into an arched configuration. For the radial six-arm structure, the magnetization orientations of the arms generated cooperative torques, transforming the planar pattern into a 3D gripper-like shape. These results disclose that spatially resolved magnetization encoding introduced at the design stage can produce diverse, preprogrammed 3D morphing behaviors under an external field, providing a programmable basis for constructing magnetically actuated functional structures.

Based on these results, we selected the radial multi-arm magnetically programmed design to build a soft robot and to evaluate its locomotion modes and magnetothermal potential on biological tissue. To demonstrate soft-robot locomotion with a simple control scheme, we adopted a single permanent magnet for actuation. We first showcased a grasping motion triggered by applying a magnetic field perpendicular to the horizontal plane (Figure 4ci and 4cii, **Video S2**). This motion could be used to envelop targeted tissue (e.g., a tumor mass) or to retrieve foreign objects. We then displayed a planar crawling gait driven by a magnetic field (Figure 4ciii and 4civ, **Video S3**). The arm at the 12 o'clock position is defined as Arm 1, and the remaining arms are numbered clockwise to Arm 6. When the magnet was laterally offset toward Arms 2 and 3 and slowly approached, the stronger field and larger gradient on that side caused Arms 2 and 3 to move downward first, forming ground-contact anchors. Due to the non-uniform field distribution, the adjacent Arms 1 and 4 exhibited an opposite out-of-plane response and lifted upward, whereas Arms 5 and 6, located in the weak-field region away from the magnet, deformed minimally. Next, we further decreased the magnet–sample distance and translated the magnet along the direction pointing from Arms 2/3. As the magnet approached, the high-gradient region moved accordingly: the grounded arms provided frictional anchoring while the rest of the body underwent relative sliding, generating a displacement and propelling the robot toward the magnet's direction of motion. Finally, when the magnet was moved away, the reduced magnetic actuation allowed the robot to recover its initial flat configuration through elastic restoration; Arms 5 and 6 remained largely unchanged throughout the cycle due to insufficient field strength. Finally, rapid reversal of the external field direction was readily achieved by flipping the permanent magnet, which induced repeated whole-body rolling/flipping of the soft robot (Figure 4cv and 4cvi, **Video S4**). This gait may be useful for overcoming obstacles or achieving vertical (z-axis) displacement.

We used handheld permanent magnets to control the motion of soft robots. While this method is simple, low-cost, and flexible, it lacks sufficient control precision. The use of a magnetic-field-driven system based on coil arrays provides a more precise means of control. Here, we present a theoretical analysis of the motion patterns of a magnetically programmable soft robot using orthogonal coil arrays. A Helmholtz coil consists of two identical coils arranged orthogonally with a spacing equal to the coil radius; when currents of equal magnitude and in the same direction are passed through the coils, a uniform magnetic field is generated (Figure 5a). For a magnetic elastomer (with magnetic induction M) placed in a magnetic field B, which is subjected to the combined effects of magnetic driving force and torque, the calculation formula is as

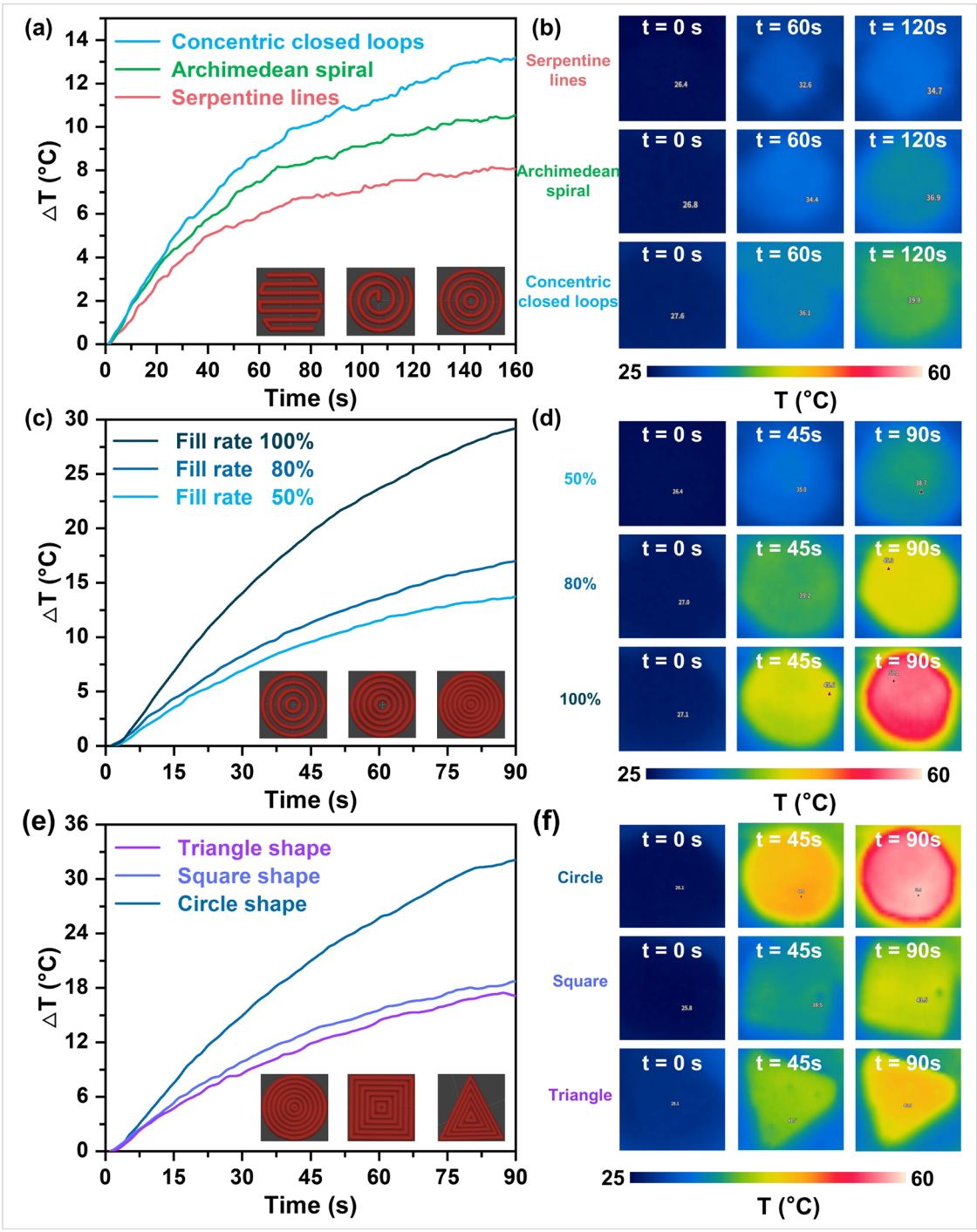

Figure 3. Comparison of heating efficiency under different printing methods ($n = 3$). (a) Temperature changes over time, and (b) infrared thermal imaging at the same time points of different printing paths. (c) Temperature changes over time, and (d) infrared thermal imaging at the same time points of different fill rates. (e) Temperature changes over time, and (f) infrared thermal imaging at the same time points of different printing shapes.

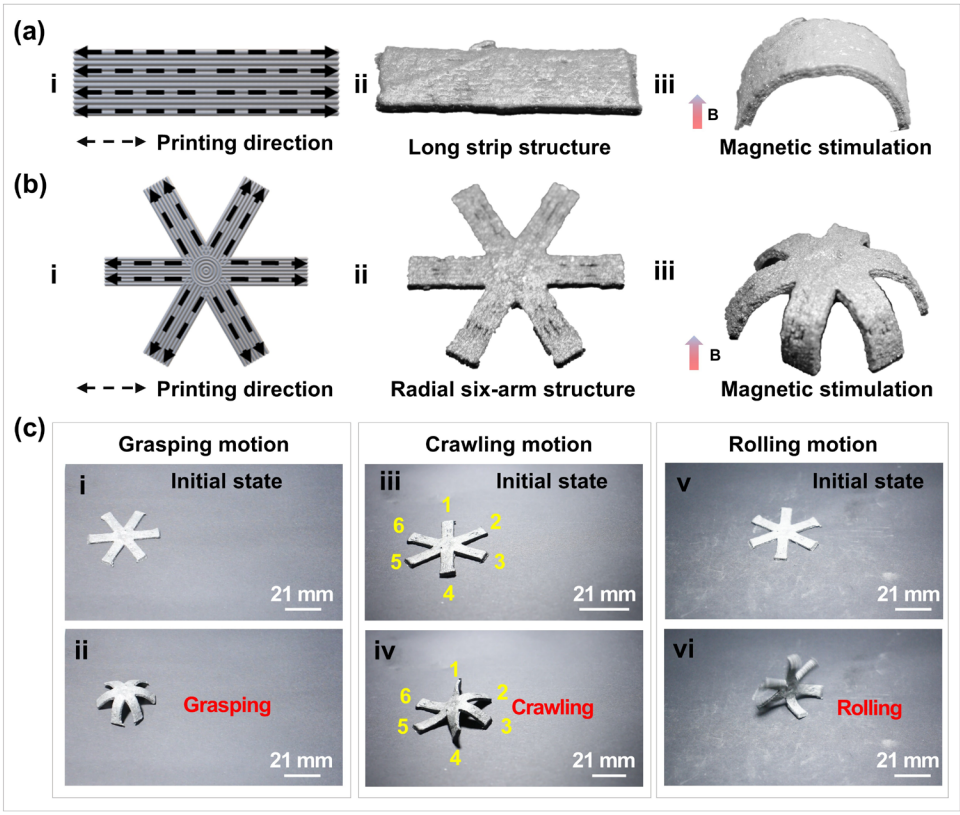

Figure 4. Different design approaches for printing structures and deformation patterns under magnetic fields. (a) Long strips with opposing printing along the long edge. (b) Radial six-arm structure. (c) Photographs of MLME soft robot motion under magnetic field control (scale bars: 21 mm; scale bars represent actual size without magnification). (i & ii) Grasping motion. (iii & iv) Crawling motion. (v & vi) Rolling motion.

follows:

$$F = \nabla(B \cdot M) \tag{5}$$

$$\tau = B \times M \tag{6}$$

Since the Helmholtz coils generate a uniform magnetic field with a magnetic field gradient of zero, a magnetic elastomer moving within this field will be subject only to the magnetic torque τ (Figure 5b). Here, we performed a motion analysis in a two-dimensional plane using a magnetically programmed strip structure as an example, in which the internal magnetic domains were oriented along the printing path. For the crawling mode, the strip adhered to the substrate surface in its initial state (Figure 5ci). When a vertical magnetic field B_z was applied, both sides of the strip experienced corresponding magnetic torques, causing the strip to arch as a whole and form a symmetrical bending configuration (Figure 5cii). By further applying a horizontal magnetic field component B_x, the force and contact symmetry on both sides of the strip were disrupted, inducing differences in the normal support forces and frictional states at both ends, thereby achieving unilateral sliding (Figure 5ciii). Subsequently, upon removal of B_x, the structure recovered, ultimately achieving a displacement along the substrate (Figure 5civ). The corresponding sequence of magnetic field application is shown in Figure 5d: first, B_z was applied and maintained to establish the primary bending, and then B_x was briefly introduced as a biasing field to achieve directionally selective motion. For the rolling mode, the strip also started from the initial adhered state (Figure 5ei). When B_x and B_z were applied in a coupled mode, the direction of the composite magnetic field continuously changed within the two-dimensional plane, and the strip exhibited a one-sided dominant flipping trend driven by magnetic torque (Figure 5eii). As the driving field further developed, the structure completed its orientation change and established a new stable contact state on the substrate

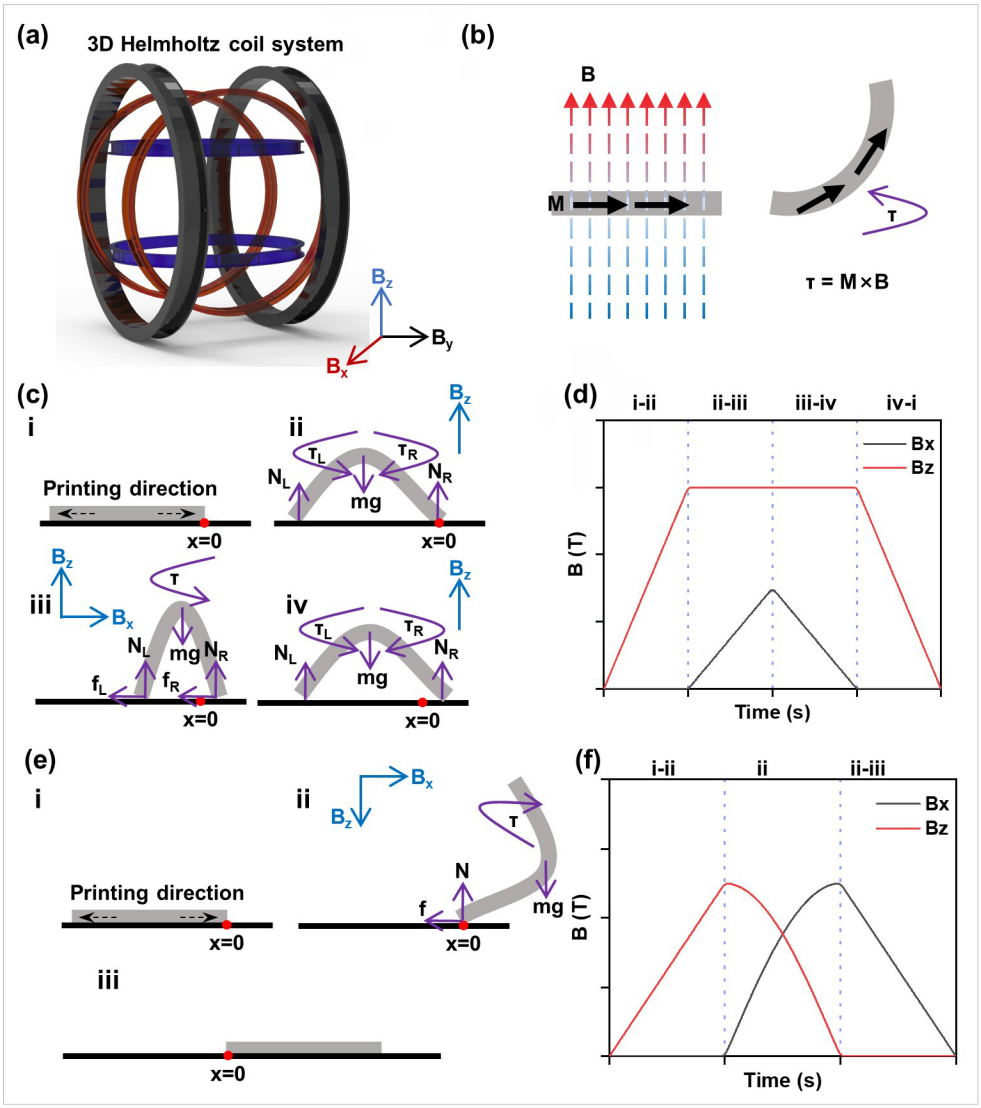

Figure 5. Schematic illustration of the motion mechanism of a magnetic soft robot driven by a coupled magnetic field. (a) Schematic diagram of a 3D Helmholtz coil system. (b) Force analysis of the strip structure under the influence of an applied uniform magnetic field. (c) Schematic diagram of the deformation and force analysis for the strip's crawling motion. (d) Magnetic field control sequence diagram corresponding to the crawling mode. (e) Schematic diagram of the deformation evolution for the strip's rolling motion. (f) Magnetic field control sequence diagram corresponding to the rolling mode.

(Figure 5eiii). This mode demonstrates that by adjusting the relative amplitudes and temporal relationships of the magnetic field components, it is possible not only to achieve translational motion of the strip structure but also to induce more complex motion behaviors, such as rolling. The corresponding control timing is shown in Figure 5f, where the temporal overlap between B_x and B_z ensures that the structure completes a directional flip while maintaining its curved state.

Furthermore, we demonstrated the feasibility of localized magnetothermal therapy on *ex vivo* porcine intestine tissue (Figure 6a, **Video S5**). Different printing paths yielded markedly distinct heating regions and temperature distributions, with the central concentric-loop region achieving a higher localized temperature rise, enabling more concentrated heating. Because direct infrared measurement of the tissue temperature field was obstructed by the tissue interface, we combined thermophysical characterization and finite-element simulations to predict tissue heating. The key simulation parameters, including those of the MLME and the intestinal tissue[31], are summarized in Table 1.

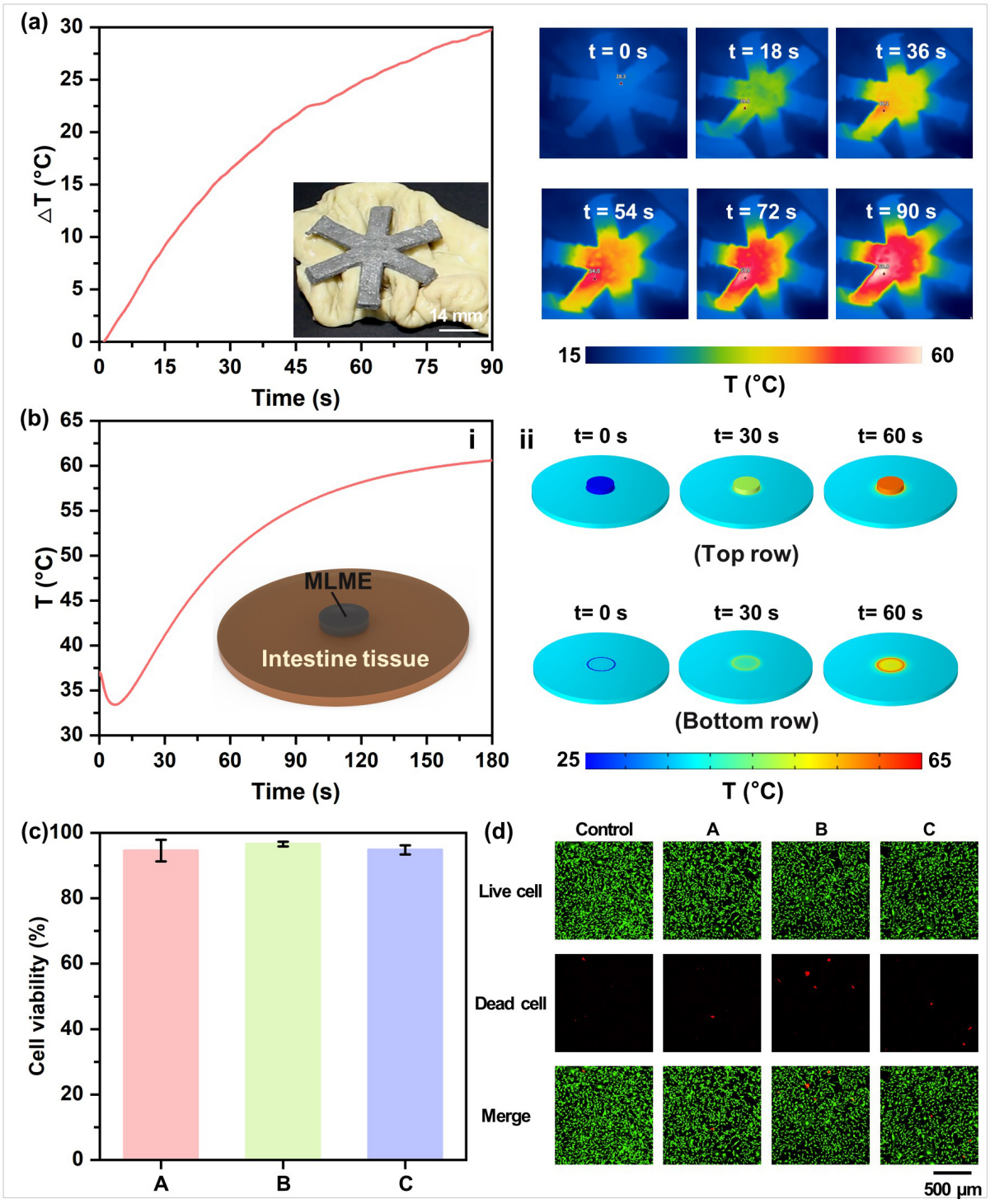

Figure 6. Localized magnetothermal therapy and *in vitro* cytotoxicity evaluation of MLME soft robot on *ex vivo* porcine intestine tissue. (a) Temperature rise curves and magnetothermal heating infrared images of MLME soft robot on *ex vivo* porcine intestine tissue (scale bar: 14 mm; scale bar represents actual size without magnification). (b) (i) Geometric model of MLME and intestinal tissue and temperature change curve at the central point on the upper surface of intestinal tissue. (ii) Temperature distribution maps for the entire model (top row) and the upper surface of intestinal tissue (bottom row). (c) Cell viability of NIH 3T3 cells after treatment with extraction media from sample A, sample B, and sample C, measured by the CCK-8 assay. (d) Live/dead staining images of NIH 3T3 cells after treatment with different sample extraction media (scale bars: 500 μm; magnifications: 10x).
Abbreviations: CCK: Cell counting kit; MLME: Magnetic liquid metal–elastomer.

The central heating region of the MLME was modeled as a cylinder with a diameter of 10 mm and a height of 2 mm, while the intestine tissue was modeled as a cylindrical tissue with a diameter of 50 mm and a height of 2 mm. The MLME was positioned at the center of the intestinal tissue (Figure 6bi). Based on the surface temperature rise data points measured on the concentric loop MLME on the insulating material substrate, we fitted a curve:

$$T = 74.7 - 49.4e^{-\frac{t}{51.06}} \quad (7)$$

where T is the temperature and t is time. Plotting the fitted curve alongside the experimental data points revealed excellent agreement (Figure S3), with a high R^2 value of 0.99972, confirming the validity of the fit. In the simulation, we assumed the thermal properties of both the MLME and intestinal tissues remained constant and numerically solved the heat transfer between them. Based on the numerical simulation results, we obtained temperature distribution maps of the MLME and intestinal tissue as a whole, as well as the intestinal tissue at different time points (Figure 6bii). The intestinal tissue surface experienced significant heating at contact points with the MLME due to the magnetothermal effect.

To further evaluate the spatial resolution of heating and the influence of thermal diffusion, we extracted the 40 °C, 50 °C, and 60 °C isothermal contours from the simulated tissue-surface temperature field and quantified their outward diffusion distances relative to the outer boundary of the circular MLME heater. The 60 °C contour remained close to the MLME outer boundary, with an outward diffusion distance of approximately 0.53 mm, indicating that the high-temperature ablation-relevant region was mainly confined near the heater–tissue contact area. In contrast, the 50 °C and 40 °C contours extended farther outward by approximately only 0.90 mm and 2.5 mm, respectively (Figure S4). This confirms its potential for precise targeted thermal ablation. Simulation temperature outputs at the central point of the MLME-tissue contact interface showed that the temperature at this point first decreased and then rapidly increased, reaching approximately 60 °C by 180 s (Figure 6bi). The initial cooling phase occurred because the MLME soft robot was at room temperature, while the subsequent process rapidly elevated the surface temperature of the intestinal tissue.

After evaluating *ex vivo* magnetothermal therapy, we further assessed the *in vitro* cytotoxicity of the main material components. Three representative samples were tested: Silicone elastomer (sample A), Silicone elastomer with Ag-coated NdFeB (sample B), and Silicone elastomer with Ag-coated NdFeB and LM (sample C, MLME). NIH 3T3 cells were cultured with the corresponding extraction media, and cell viability was quantified using the CCK-8 assay. All three groups showed high cell viability above 90%, indicating that no obvious cytotoxicity was induced by the samples under the tested conditions (Figure 6c). Consistently, live/dead staining observed by confocal microscopy showed predominantly live cells in all groups, with only scattered dead cells (Figure 6d). These results provide an initial *in vitro* validation of the cytocompatibility of the MLME composite and support its further evaluation for magnetothermal therapeutic applications.

Table 1. Parameters of MLME and intestinal tissue used in the simulations

Materials	Density (kg/m³)	Specific heat capacity (J/kg/K)	Thermal conductivity (W/m/K)
MLME	3,303	483.2	0.7998
Intestinal tissue	1,100	3,375	0.461

Abbreviation: MLME: Magnetic liquid metal–elastomer.

4. Conclusion

In this work, we propose and validate a magnetic-field-assisted 3D printing strategy for the programmable fabrication of MLME. The approach enables stable conductive interconnection without an additional post-sintering step through field-induced cooperative coalescence of droplets, while simultaneously allowing spatial encoding of magnetic domains during printing via a local alignment field—a capability that results in predictable 3D morphing. To enhance magnetothermal heating efficiency, we derived a path-dependent geometry factor from eddy-current loss and used it to optimize printing paths and shapes. Experiments showed that optimized concentric closed-loop paths markedly improved temperature-rise efficiency under AMFs. The

resulting soft robot achieved grasping, crawling, and rolling under single-magnet actuation and demonstrated localized heating of *ex vivo* intestinal tissue, highlighting the platform's potential for minimally invasive magnetic actuation-assisted magnetothermal therapy.

Several aspects of this study warrant further investigation. First, current locomotion demonstrations rely on manual manipulation of a single permanent magnet; future work could integrate multi-coil electromagnetic systems to generate controllable 3D vector fields and gradients, enabling more precise navigation and richer deformation modes. For *in vivo* translation, such magnetic control should be further combined with image-guided navigation and retrieval strategies, because wireless soft robotic medical devices must overcome biological barriers while maintaining controllability and safety in confined anatomical environments. In particular, dynamic biological conditions, including luminal fluid flow, gastrointestinal peristalsis, mucus-covered interfaces, and tissue deformation, may alter robot–tissue friction, passive displacement, anchoring stability, and the contact state required for localized magnetothermal heating. Therefore, future studies should evaluate the MLME robot in dynamic tissue-mimicking models and animal models that reproduce these physiological constraints.

Second, the *ex vivo* tissue model does not account for *in vivo* perfusion cooling, tissue heterogeneity, or complex tumor boundaries. Therefore, the next translational step should involve dynamic tissue-mimicking models and animal models that reproduce physiological constraints, such as luminal flow, peristaltic motion, tissue deformation, and heterogeneous thermophysical properties. For magnetothermal therapy, perfusion-aware bioheat transfer models and image-based anatomical reconstruction should be incorporated to predict the thermal dose and delineate ablation margins more accurately. Closed-loop temperature monitoring will also be important to avoid overheating of surrounding healthy tissues. Additionally, more comprehensive biocompatibility evaluations, including hemocompatibility, long-term degradation/leakage analysis, and *in vivo* safety assessment, are still required before clinical translation. Furthermore, the current printing mode of the robot is *ex vivo*; future interventional *in vivo* 3D printing may become possible. Finally, the integration of artificial intelligence technology is expected to further enhance design and manufacturing processes and enable intelligent, high-precision navigation in complex environments.[32] Overall, magnetic-field-assisted LM 3D printing provides a manufacturable, designable, and scalable foundation for magnetically programmed soft robots toward personalized medicine (Figure 7).

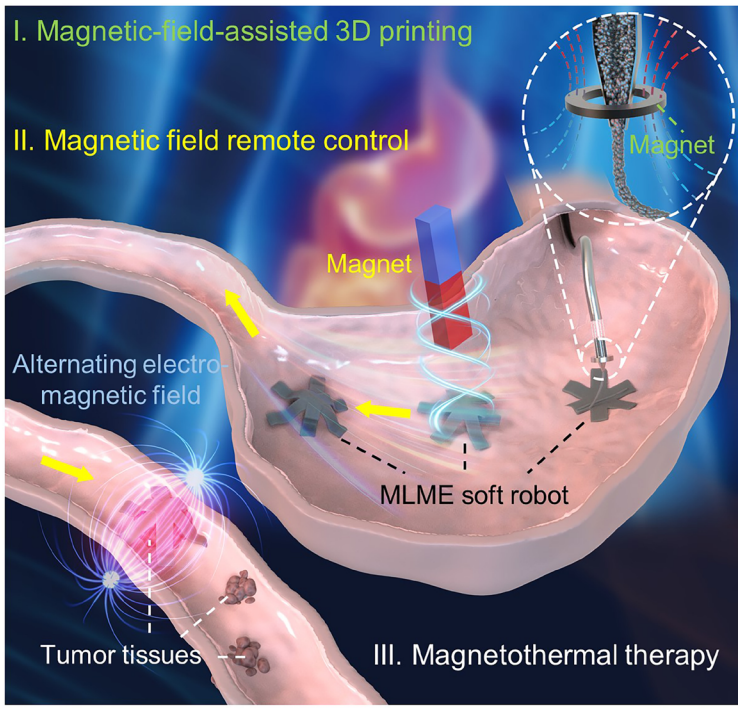

Figure 7. Envisioned potential application of magnetically programmable 3D-printed liquid metal robots for non-contact magnetic navigation and magnetothermal tumor therapy in future targeted treatment
Abbreviation: MLME: Magnetic liquid metal–elastomer.

Acknowledgments

None.

Funding

The work is partially supported by the National Natural Science Foundation of China (no. 52506093, no. 52203360) and the Tsinghua IDG/McGovern "Brain+X" Seed Grant Doctoral and Postdoctoral Program.

Conflict of interest

Xiyu Zhu is an employee of SINOPEC but was not involved in any activities that could constitute a conflict of interest in relation to this study. All other authors declare no competing interests.

Author contributions

Conceptualization: Weichen Feng, Xiaohui Shan, Jing Liu
Formal analysis: Weichen Feng, Xiaohui Shan, Bo Wang, Xiyu Zhu, Bo Yuan
Methodology: Weichen Feng, Xiaohui Shan, Bo Wang, Xiyu Zhu, Bo Yuan
Investigation: Weichen Feng, Xiaohui Shan, Bo Wang, Xiyu Zhu, Bo Yuan
Writing–original draft: Weichen Feng, Minghui Guo, Jianye Gao
Writing–review & editing: Jianye Gao, Jing Liu

Ethics approval and consent to participate

Not applicable.

Consent for publication

Not applicable.

Availability of data

All the data generated or analyzed during this study are included in this published article and its supplementary information files.

References

1. Ciuti G, Webster RJ, Kwok KW, Menciassi A. Robotic surgery. *Nat Rev Bioeng*. 2025;3(7):565-578.

   doi: 10.1038/s44222-025-00294-6

2. Dupont PE, Nelson BJ, Goldfarb M, *et al.* A decade retrospective of medical robotics research from 2010 to 2020. *Sci Robot*. 2021;6(60):eabi8017.

   doi: 10.1126/scirobotics.abi8017

3. Wang N, Ying Y, Wang W, Liu J, Wu D, Zhao Y. Intelligent sensing and measurement technologies for medical robotics: A review. *Sens Actuator A-Phys*. 2025;394:116956.

   doi: 10.1016/j.sna.2025.116956

4. Murphy RR. Is it safe to hug a robot like Baymax? *Sci Robot*. 2022;7(70):eade5835.

   doi: 10.1126/scirobotics.ade5835

5. Dhawan V, Wu B, Narayanan S, Shi D, Patel Y, Cui X. A comparative study assessing neural recording quality and inflammatory tissue response between stiff and flexible microelectrode arrays. *Biomaterials*. 2026;329:123929.

   doi: 10.1016/j.biomaterials.2025.123929

6. Cianchetti M, Laschi C, Menciassi A, Dario P. Biomedical applications of soft robotics. *Nat Rev Mater*. 2018;3(6):143-153.

doi: 10.1038/s41578-018-0022-y

7. Yin S, Yao DR, Song Y, *et al.* Wearable and implantable soft robots. *Chem Rev.* 2024;124(20):11585-11636.

   doi: 10.1021/acs.chemrev.4c00513

8. Zhou S, Li Y, Wang Q, Lyu Z. Integrated actuation and sensing: Toward intelligent soft robots. *Cyborg Bionic Syst*. 2024;5:0105.

   doi: 10.34133/cbsystems.0105

9. Malappuram KM, Chatterjee K, Homer-Vanniasinkam S, Nain A. Clinical challenges in soft robotics. *Adv Robot Res*. 2025;1(2):202400018.

   doi: 10.1002/adrr.202400018

10. Wang T, Wu Y, Yildiz E, Kanyas S, Sitti M. Clinical translation of wireless soft robotic medical devices. *Nat Rev Bioeng*. 2024;2(6):470-485.

    doi: 10.1038/s44222-024-00156-7

11. Chung WG, Kim E, Kwon YW, *et al.* Ga-based liquid metals: Versatile and biocompatible solutions for next-generation bioelectronics. *Adv Funct Mater*. 2024;34(31):307990.

    doi: 10.1002/adfm.202307990

12. Chen S, Zhao R, Sun X, Wang H, Li L, Liu J. Toxicity and biocompatibility of liquid metals. *Adv Healthc Mater*. 2023;12(3):2201924.

    doi: 10.1002/adhm.202201924

13. Wu D, Wu S, Narongdej P, *et al.* Fast and facile liquid metal printing via projection lithography for highly stretchable electronic circuits. *Adv Mater*. 2024;36(34):2307632.

    doi: 10.1002/adma.202307632

14. Lee S, Chung WG, Jeong H, *et al.* Electrophysiological analysis of retinal organoid development using 3D microelectrodes of liquid metals. *Adv Mater*. 2024;36(35):2404428.

    doi: 10.1002/adma.202404428

15. Guo Z, Jin D, Li H, *et al.* Liquid metal amplified charge separation in photocatalytic micro/nanomotors for antibacterial therapy. *ACS Nano*. 2025;19(21):20037-20050.

doi: 10.1021/acsnano.5c03785

16. Liu L, Rahim MA, Li T, *et al.* Composites from self-assembled protein nanofibrils and liquid metal gallium. *Adv Funct Mater*. 2024;34(45):2405918.

    doi: 10.1002/adfm.202405918

17. Cao L, Yu D, Xia Z, *et al.* Ferromagnetic liquid metal putty-like material with transformed shape and reconfigurable polarity. *Adv Mater*. 2020;32(17):2000827.

    doi: 10.1002/adma.202070136

18. Xiang W, Lu Y, Wang H, *et al.* Liquid-metal-based magnetic fluids. *Nat Rev Mater*. 2024;9(6):433-449.

    doi: 10.1038/s41578-024-00679-w

19. Shen Y, Cao J, Zhou E, *et al.* Tough hydrogel-coated containment capsule of magnetic liquid metal for remote gastrointestinal operation. *Natl Sci Rev*. 2025;12(4):nwaf042.

    doi: 10.1093/nsr/nwaf042

20. Wang D, Wu Q, Guo R, Lu C, Niu M, Rao W. Magnetic liquid metal loaded nano-in-micro spheres as fully flexible theranostic agents for SMART embolization. *Nanoscale*. 2021;13(19):8817-8836.

    doi: 10.1039/D1NR01268A

21. Shen Y, Jin D, Fu M, *et al.* Reactive wetting enabled anchoring of non-wettable iron oxide in liquid metal for miniature soft robot. *Nat Commun*. 2023;14(1):6276.

    doi: 10.1038/s41467-023-41920-4

22. Shan X, Feng W, Cui Z, *et al.* Ubiquitous liquid metal 3D printing: From gas, liquid to rigid media. *Adv Funct Mater*. 2025;35(16):2421571.

    doi: 10.1002/adfm.202421571

23. Shan X, Feng W, Guo M, Wang X, Liu J. Pan-media liquid metal 3D printing. *Innovation*. 2025;6(4):100813.

    doi: 10.1016/j.xinn.2025.100813

24. Ryoo M, Kim D, Noh J, Ahn S. 3D-printed electronics for biomedical applications. *Int J Bioprint*. 2024;10(6):4139.

    doi: 10.36922/ijb.4139

25. Zhao R, Wang H, Shi Y, Zhu Z, Zhang B. Low-temperature manufacturable, recyclable, and reconfigurable liquid-metal bonded NdFeB magnets for sensors and robotics. *AIP Adv*. 2024;14(1):015061.

    doi: 10.1063/5.0175503

26. Chen G, Ma B, Zhang J, Chen Yi, Liu H. Reprogrammable magnetic soft robots based on low melting alloys. *Adv Intell Syst*. 2023;5(10):2300173.

    doi: 10.1002/aisy.202300173

27. Kim Y, Yuk H, Zhao R, Chester S, Zhao X. Printing ferromagnetic domains for untethered fast-transforming soft materials. *Nature*. 2018;558(7709):274-279.

    doi: 10.1038/s41586-018-0185-0

28. Hoang TT, Phan PT, Thai MT, *et al.* Magnetically engineered conductivity of soft liquid metal composites for robotic, wearable electronic, and medical applications. *Adv Intell Syst*. 2022;4(12):2200282.

    doi: 10.1002/aisy.202200282

29. Lee S, Jaseem SA, Atar N, *et al.* Connecting the dots: Sintering of liquid metal particles for soft and stretchable conductors. *Chem Rev*. 2025;125(6):3551-3585.

    doi: 10.1021/acs.chemrev.4c00850

30. Lu Y, Yu D, Dong H, *et al.* Dynamic leakage-free liquid metals. *Adv Funct Mater*. 2023;33(11):2210961.

    doi: 10.1002/adfm.202210961

31. Cao Y, Fan L, Gao J, *et al.* Magnetic and injectable Fe-doped liquid metals for controlled movement and photothermal/electromagnetic therapy. *J Mat Chem B*. 2024;12(9):2313-2323.

    doi: 10.1039/D3TB02501B

32. Liu J, Wang Q, Xu K, Li Z, Liu J. AI-enhanced magnetically controlled 4D printing: Reshaping the future of medical robotics. *Int J Bioprint*. 2025;11(6):197-204.

    doi: 10.36922/IJB025420427